J. Fluid Mech. (2021), *vol.* 917, A6, doi:10.1017/jfm.2021.262

Regime transitions in thermally driven high-Rayleigh number vertical convection

Qi Wang[1,2], **Hao-Ran Liu**[1], **Roberto Verzicco**[1,3,4], **Olga Shishkina**[5,†]
and Detlef Lohse[1,5,†]

[1]Physics of Fluids Group and Max Planck Center for Complex Fluid Dynamics, MESA+ Institute and J. M. Burgers Centre for Fluid Dynamics, University of Twente, P.O. Box 217, 7500AE Enschede, The Netherlands

[2]Department of Modern Mechanics, University of Science and Technology of China, 230027 Hefei, PR China

[3]Dipartimento di Ingegneria Industriale, University of Rome 'Tor Vergata', Via del Politecnico 1, Roma 00133, Italy

[4]Gran Sasso Science Institute - Viale F. Crispi, 767100 L'Aquila, Italy

[5]Max Planck Institute for Dynamics and Self-Organization, 37077 Göttingen, Germany

(Received 30 November 2020; revised 19 January 2021; accepted 15 March 2021)

Thermally driven vertical convection (VC) – the flow in a box heated on one side and cooled on the other side, is investigated using direct numerical simulations with Rayleigh numbers over the wide range of $10^7 \leq Ra \leq 10^{14}$ and a fixed Prandtl number $Pr = 10$ in a two-dimensional convection cell with unit aspect ratio. It is found that the dependence of the mean vertical centre temperature gradient S on Ra shows three different regimes: in regime I ($Ra \lesssim 5 \times 10^{10}$), S is almost independent of Ra; in the newly identified regime II ($5 \times 10^{10} \lesssim Ra \lesssim 10^{13}$), S first increases with increasing Ra (regime II$_a$), reaches its maximum and then decreases again (regime II$_b$); and in regime III ($Ra \gtrsim 10^{13}$), S again becomes only weakly dependent on Ra, being slightly smaller than in regime I. The transition from regime I to regime II is related to the onset of unsteady flows arising from the ejection of plumes from the sidewall boundary layers. The maximum of S occurs when these plumes are ejected over approximately half of the area (downstream) of the sidewalls. The onset of regime III is characterized by the appearance of layered structures near the top and bottom horizontal walls. The flow in regime III is characterized by a well-mixed bulk region owing to continuous ejection of plumes over large fractions of the sidewalls, and, as a result of the efficient mixing, the mean temperature gradient in the centre S is smaller than that of regime I. In the three different regimes, significantly different

---

† Email addresses for correspondence: olga.shishkina@ds.mpg.de, d.lohse@utwente.nl

flow organizations are identified: in regime I and regime II_a, the location of the maximal horizontal velocity is close to the top and bottom walls; however, in regime II_b and regime III, banded zonal flow structures develop and the maximal horizontal velocity now is in the bulk region. The different flow organizations in the three regimes are also reflected in the scaling exponents in the effective power law scalings $Nu \sim Ra^{\beta}$ and $Re \sim Ra^{\gamma}$. Here, Nu is the Nusselt number and Re is the Reynolds number based on maximal vertical velocity (averaged over vertical direction). In regime I, the fitted scaling exponents ($\beta \approx 0.26$ and $\gamma \approx 0.51$) are in excellent agreement with the theoretical predictions of $\beta = 1/4$ and $\gamma = 1/2$ for laminar VC (Shishkina, *Phys. Rev.* E., vol. 93, 2016, 051102). However, in regimes II and III, β increases to a value close to 1/3 and γ decreases to a value close to 4/9. The stronger Ra dependence of Nu is related to the ejection of plumes and the larger local heat flux at the walls. The mean kinetic dissipation rate also shows different scaling relations with Ra in the different regimes.

Key words: convection in cavities

1. Introduction

Thermally driven convective fluid motions are ubiquitous in various geophysical and astrophysical flows, and are important in many industrial applications. Rayleigh–Bénard convection (RBC) (Ahlers, Grossmann & Lohse 2009; Lohse & Xia 2010; Chillà & Schumacher 2012; Xia 2013), where a fluid layer in a box is heated from below and cooled from above, and vertical convection (VC) (Ng *et al.* 2015; Shishkina 2016; Ng *et al.* 2017, 2018), where the fluid is confined between two differently heated isothermal vertical walls, have served as two classical model problems to study thermal convection. Vertical convection was also called convection in a differentially heated vertical box in many early papers (Paolucci & Chenoweth 1989; Le Quéré & Behnia 1998). Both RBC and VC can be viewed as extreme cases of the more general so-called tilted convection (Guo *et al.* 2015; Shishkina & Horn 2016; Wang *et al.* 2018*a*,*b*; Zwirner & Shishkina 2018; Zwirner *et al.* 2020; Zhang, Ding & Xia 2021), with a tilt angle of 0° for RBC and 90° for VC. We focus on VC in this study. Vertical convection finds many applications in engineering, such as thermal insulation using double-pane windows or double walls, horizontal heat transport in water pools with heated/cooled sidewalls, crystal growth procedures, nuclear reactors, ventilation of rooms, and cooling of electronic devices, to name only a few. Vertical convection has also served as a model to study thermally driven atmospheric circulation (Hadley 1735; Lappa 2009) or thermally driven circulation in the ocean, e.g. next to an ice-block (Thorpe, Hutt & Soulsby 1969; Tanny & Tsinober 1988).

The main control parameters in VC are the Rayleigh number $Ra \equiv g\alpha L^3 \Delta/(\nu\kappa)$ and the Prandtl number $Pr \equiv \nu/\kappa$. Here, α, ν and κ are the thermal expansion coefficient, the kinematic viscosity and the thermal diffusivity of the convecting fluid, respectively, g is the gravitational acceleration, $\Delta \equiv T_h - T_c$ is the temperature difference between the two side walls, and L is the width of the convection cell. The aspect ratio $\Gamma \equiv H/L$ is defined as the ratio of height H over width L of the domain. The responses of the system are characterized by the Nusselt number $Nu \equiv QL/(k\Delta)$ and the Reynolds number $Re \equiv UL/\nu$, which indicate the non-dimensional heat transport and flow strength in the system, respectively. Here Q is the heat flux crossing the system and U is the characteristic velocity of the flow.

Since the pioneering work of Batchelor (Batchelor 1954), who first addressed the case of steady-state heat transfer across double-glazed windows, VC has drawn significant attention especially in the 1980s and 1990s, and most of these studies used experiments or a two-dimensional (2-D) direct numerical simulation (DNS) in a square domain with unit aspect ratio. For relatively low Ra (e.g. $Ra < 10^3$), the flow is weak and heat is transferred mainly by thermal conduction. With increasing Ra, typical stratified flow structures appear in the bulk region (de Vahl Davis & Jones 1983), while the flow remains steady. With a further increase in Ra, the flow becomes unsteady with periodical/quasi-periodical or chaotic motions (Paolucci & Chenoweth 1989; Le Quéré & Behnia 1998), and eventually becomes turbulent when Ra is sufficiently high (Paolucci 1990).

The onset of unsteadiness has been well explored in the past (Chenoweth & Paolucci 1986; Paolucci & Chenoweth 1989; Janssen & Henkes 1995; Le Quéré & Behnia 1998). Paolucci & Chenoweth (1989) investigated the influence of the aspect ratio $\varGamma$ on the onset of unsteadiness for 2-D VC with $Pr = 0.71$. They found that for $\varGamma \gtrsim 3$, the first transition from the steady state arises from an instability of the sidewall boundary layers, while for smaller aspect ratios $0.5 \leq \varGamma \lesssim 3$, it arises from internal waves near the departing corners. Such oscillatory instability arising from internal waves was first reported by Chenoweth & Paolucci (1986). Paolucci & Chenoweth (1989) also found that for $\varGamma = 1$, the critical Rayleigh number Ra_c for the onset of unsteadiness lies between 1.8×10^8 and 2×10^8. Later work, with $Pr = 0.71$ and $\varGamma = 1$ by Le Quéré & Behnia (1998), also showed that the internal gravity waves play an important role in the time-dependent dynamics of the solutions, and $1.81 \times 10^8 \leq Ra_c \leq 1.83 \times 10^8$ was determined to be the range of the critical Rayleigh number. Janssen & Henkes (1995) studied the influence of Pr on the instability mechanisms for $\varGamma = 1$, and observed that for $0.25 \leq Pr \leq 2$, the transition occurs through periodic and quasi-periodic flow regimes. One bifurcation is related to an instability occurring in a jet-like fluid layer exiting from the corners of the cavity where the vertical boundary layers are turned horizontal. Such jet-like flow structures are responsible for the generation of internal gravity waves (Chenoweth & Paolucci 1986; Paolucci & Chenoweth 1989). The other bifurcation occurs in the boundary layers along the vertical walls. Both of these instabilities are mainly shear-driven. For $2.5 \leq Pr \leq 7$, Janssen & Henkes (1995) found an 'immediate' (i.e. sharp) transition from the steady to the chaotic flow regime, without intermediate regimes. This transition is also caused by boundary layer instabilities. They also showed that Ra_c significantly increases with increasing Pr, e.g. for $Pr = 4$, the flow can still be steady with $Ra = 2.5 \times 10^{10}$. However, owing to the computation limit, unsteady motions for the large-Pr cases have largely remained unexplored in the past.

Additionally, the flow structures for VC have been examined in detail. A typical flow feature for VC is the stably-stratified bulk region (de Vahl Davis & Jones 1983; Ravi, Henkes & Hoogendoorn 1994; Trias *et al.* 2007; Sebilleau *et al.* 2018; Chong *et al.* 2020). Such stratification can be quantified by the time-averaged non-dimensional temperature gradient at the centre, namely

$$S \equiv \langle (L/\varDelta)(\partial T/\partial z)_c \rangle_t \, . \tag{1.1}$$

Here $\langle\rangle_t$ denotes a time average. Gill (1966) derived asymptotic solutions for high Pr, and predicted $S = 0.42$ as $Ra \rightarrow \infty$, while an accurate solution of the same system by Blythe, Daniels & Simpkins (1983) predicted a value of 0.52. Later DNS results for $Ra = 10^8$ and $Pr = 70$ yielded $S = 0.52$ (Ravi *et al.* 1994), which is in excellent agreement with the theoretical prediction by Blythe *et al.* (1983). However, for small Pr, the structure of the core and the vertical boundary layer are no longer similar to those predicted by the asymptotic solutions which are valid for large Pr (Blythe *et al.* 1983). Unfortunately, there exists no such asymptotic theory for finite Pr. Only Graebel (1981) has presented some approximate solutions, in which some terms have been neglected in the equations. For $Pr = 0.71$, his prediction yielded $S = 0.49$, which is considerably smaller than the value $S \approx 1$ from DNS (Ravi *et al.* 1994; Trias *et al.* 2007). It was concluded that S is independent of Ra for $Ra \leq 10^{10}$ (Paolucci 1990); however, it is evident that the dependence of S on Ra and Pr, especially for those with high $Ra > 10^{10}$ and low $Pr < 0.71$, is still poorly understood.

A key question in the study of thermal convection is: How do Nu and Re depend on Ra and Pr? This question has been extensively addressed in RBC over the past years (Ahlers *et al.* 2009). For RBC, the mean kinetic dissipation rate (ϵ_u) and thermal dissipation rate (ϵ_θ) obey exact global balances, which feature Ra, Nu and Pr (Shraiman & Siggia 1990). For this problem, in a series of papers, Grossmann & Lohse (2000, 2001, 2002, 2004) developed a unifying theory to account for $Nu(Ra, Pr)$ and $Re(Ra, Pr)$ over wide parameter ranges. The central idea of the theory is a decomposition of ϵ_u and ϵ_θ into their boundary layer and bulk contributions. The theory has been well confirmed through various experiments and numerical simulations (Stevens *et al.* 2013). This theory has also been applied to horizontal convection (Shishkina, Grossmann & Lohse 2016; Shishkina & Wagner 2016) and internally heated convection (Wang, Shishkina & Lohse 2020*b*). However, in VC, the exact relation for ϵ_u does not hold, which impedes the applicability of the unifying theory to the scalings in VC (Ng *et al.* 2015).

As compared with RBC, for VC, much less work has been devoted to the dependences $Nu(Ra, Pr)$ and $Re(Ra, Pr)$. Past studies have suggested power law dependences, i.e. $Nu \sim Ra^\beta$ and $Re \sim Ra^\gamma$, at least in a certain Ra range. The reported scaling exponent β was found to vary from 1/4 to 1/3 (Xin & Le Quéré 1995; Le Quéré & Behnia 1998; Trias *et al.* 2007, 2010; Ng *et al.* 2015; Shishkina 2016; Wang *et al.* 2019; Ng *et al.* 2020), depending on the Ra range and Pr. Ng *et al.* (2015) simulated three-dimensional (3-D) VC with periodic conditions in the range $10^5 \leq Ra \leq 10^9$ with $Pr = 0.709$, and obtained $\beta = 0.31$ as the considered range. For much larger $Pr \gg 1$ and using laminar boundary layer theories, Shishkina (2016) theoretically derived $Nu \sim Ra^{1/4}$ and $Re \sim Ra^{1/2}$. These theoretical results are in excellent agreement with direct numerical simulations for Ra from 10^5 to 10^{10} in a cylindrical container with aspect ratio $\varGamma = 1$. The power law exponents $\beta = 1/4$ and $\gamma = 1/2$ were also confirmed by the DNS of Ng *et al.* (2020) in a 3-D cell with span-wise periodic boundary conditions for $10^8 \leq Ra \leq 1.3 \times 10^9$. For 2-D VC, past studies with $Ra \leq 10^{10}$ have also shown that β is closer to 1/4 than 1/3 (Xin & Le Quéré 1995; Trias *et al.* 2007, 2010; Wang *et al.* 2019). Wang *et al.* (2019) simulated 2-D VC over $10^5 \leq Ra \leq 10^9$ for fixed $Pr = 0.71$, and found $\beta \approx 0.27$ and $\gamma \approx 0.50$.

Most of the simulations for VC were conducted for $Ra \lesssim 10^{10}$. The high-Ra simulations become stiff owing to a decrease in the boundary-layer thicknesses with increasing Ra. As a result, little is known about what will happen at Ra much larger than 10^{10}. In this study, we attempt to fill this gap in knowledge by performing DNS up to $Ra = 10^{14}$. The price we have to pay is that for such large Ra, we are restricted to 2-D.

The main questions we want to address in this study are as follows.

(i) Is the conclusion that S is independent of Ra for $Ra \leq 10^{10}$ (Paolucci 1990) still valid for Ra much larger than 10^{10}?

(ii) How does the global flow organization (mean temperature and velocity profiles) change with increasing Ra up to 10^{14}?

(iii) How robust are the laminar scaling relations $Nu \sim Ra^{1/4}$ and $Re \sim Ra^{1/2}$ (Shishkina 2016) for higher Ra? Will new scaling relations appear for Ra much larger than 10^{10}?

We find that S is not independent of Ra over the studied parameter range at all. Instead, we find that apart from the small-Ra regime (now called regime I), where S only weakly depends on Ra (Paolucci 1990), there are additional regimes for $Ra \gtrsim 5 \times 10^{10}$ with different scaling relations. In regime II ($5 \times 10^{10} \lesssim Ra \lesssim 10^{13}$), with increasing Ra, S first increases (regime II$_a$) to its maximum and then decreases (regime II$_b$) again. In regime III ($Ra \gtrsim 10^{13}$), S again becomes weakly dependent on Ra, with a smaller value than that of regime I. Furthermore, we find that the laminar power law exponents $\beta = 1/4$ and $\gamma = 1/2$ undergo sharp transitions to $\beta \approx 1/3$ and $\gamma \approx 4/9$ when $Ra \gtrsim 5 \times 10^{10}$, i.e. at the transition from regime I to regime II.

The rest of the paper is organized as follows. Section 2 describes the governing equations and numerical methods. The different flow organizations in the different regimes are studied in § 3. In § 4, we discuss the transition of the scaling relations for heat and momentum transport between the different regimes. Finally, § 5 contains a summary and an outlook.

2. Numerical procedures

A sketch of 2-D VC is shown in figure 1. The top and bottom walls are insulated. The left wall is heated with temperature T_h, while the right wall is cooled with temperature T_c. No-slip and no-penetration velocity boundary conditions are used at all the walls. The aspect ratio $\varGamma \equiv H/L$ is fixed to 1. The dimensionless governing equations are the incompressible Navier–Stokes equations with an Oberbeck–Boussinesq approximation:

$$\nabla \cdot \boldsymbol{u} = 0, \tag{2.1}$$

$$\frac{\partial \boldsymbol{u}}{\partial t} + \boldsymbol{u} \cdot \nabla \boldsymbol{u} = -\nabla p + \sqrt{\frac{Pr}{Ra}} \nabla^2 \boldsymbol{u} + \theta \boldsymbol{e}_z, \tag{2.2}$$

$$\frac{\partial \theta}{\partial t} + \boldsymbol{u} \cdot \nabla \theta = \frac{1}{\sqrt{RaPr}} \nabla^2 \theta. \tag{2.3}$$

Here $\boldsymbol{e}_z$ is the unit vector pointing in the direction opposite to gravity. The dimensionless velocity, temperature and pressure are represented by $\boldsymbol{u} \equiv (u, w)$, θ and p, respectively. For non-dimensionalization, we use the width of the convection cell L and the free-fall velocity $U = (g\alpha \Delta L)^{1/2}$. Temperature is non-dimensionalized as $\theta = (T - T_c)/\varDelta$.

The governing equations were solved using the second-order staggered finite-difference code AFiD (Verzicco & Orlandi 1996; van der Poel *et al.* 2015). The code has already been extensively used to study RBC (Wang *et al.* 2020*a*,*c*; Liu *et al.* 2021) and internally heated convection (Wang *et al.* 2020*b*). Direct numerical simulation was performed for $10^7 \leq Ra \leq 10^{14}$ with a fixed $Pr = 10$. Stretched grids were used to resolve the thin boundary layers and adequate resolutions were ensured to resolve the small scales of turbulence (Shishkina *et al.* 2010). Grids with up to 8192×8192 nodes were used for the highest $Ra = 10^{14}$. We performed careful grid independence checks for several high-Ra cases. It was found that the difference of Nu and Re for the different grids were always smaller than 1 % and 2 %, respectively. Details on the simulations are provided in table 2 in the appendix.

3. Global flow organization

3.1. *Global flow fields*

We first focus on the change of global flow organizations with increasing Ra. Figure 2 shows instantaneous temperature, horizontal velocity (u) and vertical velocity (w) fields

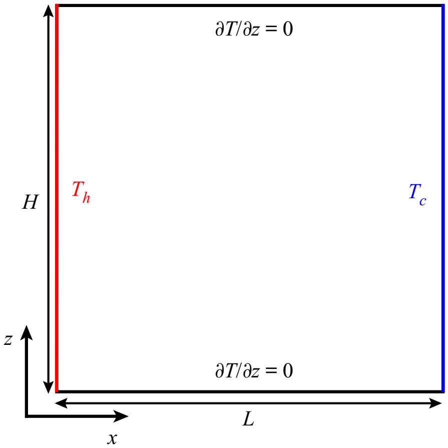

Figure 1. Sketch of two-dimensional vertical convection with unit aspect ratio. The left vertical wall is heated ($T = T_h$), while the right vertical wall is cooled ($T = T_c$), and the temperature difference is $\varDelta = T_h - T_c$. The top and bottom walls are adiabatic. All the walls have no-slip and no-penetration velocity boundary conditions.

for different *Ra*. For the considered $Pr = 10$, we find that the flow is still steady for $Ra = 5 \times 10^{10}$, as shown in figure 2(*a–c*), which is consistent with the finding that the critical Rayleigh number Ra_c for the onset of unsteadiness increases with increasing *Pr* and that the flow is indeed still steady for $Ra = 2.5 \times 10^{10}$ with $Pr = 4$ (Janssen & Henkes 1995). This is in sharp contrast with RBC, where the flow is already turbulent for such high *Ra* with $Pr = 10$ (Wang *et al.* 2020*c*). The flow is stably stratified in the bulk region, as shown in figure 2(*a*). The large horizontal velocity regions mainly concentrate near the top and bottom walls (figure 2*b*), while the strong vertical motion mainly occurs near the two sidewalls (figure 2*c*). Such flow structures are typical for steady VC with large *Pr* (Ravi *et al.* 1994).

However, with a minor increase of *Ra* from $Ra = 5 \times 10^{10}$ to $Ra = 6 \times 10^{10}$, the flow becomes instantaneously chaotic, as shown in figure 2(*d–f*). This finding is consistent with the previous result that for $Pr \geq 2.5$, there is an immediate transition from the steady to the chaotic flow regime without intermediate regimes (Janssen & Henkes 1995). This transition is caused by boundary layer instabilities, which are reflected in the plume ejections in the downstream of the boundary layers (figure 2*d*). The strong horizontal/vertical fluid motions still concentrate near the horizontal/vertical walls, as indicated in figures 2(*e*) and 2(*f*). However, there are already some chaotic features appearing in the bulk, which suggest a change of the bulk properties.

When *Ra* is further increased to 6×10^{11} (figure 2*g–i*), further evident changes of the global flow organization appear as follows. (i) The hot plumes mainly eject over the upper half of the hot sidewall, and enter the upper half of the bulk region. This makes the hot upper bulk region more isothermal than in the smaller-*Ra* cases. Similar processes happen for the cold plumes and the lower cold bulk region. Therefore, figure 2(*g*) clearly shows a larger centre temperature gradient than those in figures 2(*a*) and 2(*d*). (ii) The strong horizontal motions now not only occur near the horizontal walls, but also in the bulk region (figure 2*h*), and alternating rightward and leftward 'zonal flow' structures appear.

For the highest $Ra = 10^{14}$ (figure 2*j–l*), the thermal driving is so strong that hot plumes are now ejected over large fractions of the left vertical wall ($0.2 \lesssim z/L \lesssim 1$). The plumes are transported into the bulk region by the zonal flow structures shown in figure 2(*k*). This process causes efficient mixing in the bulk, which then leads to a smaller centre

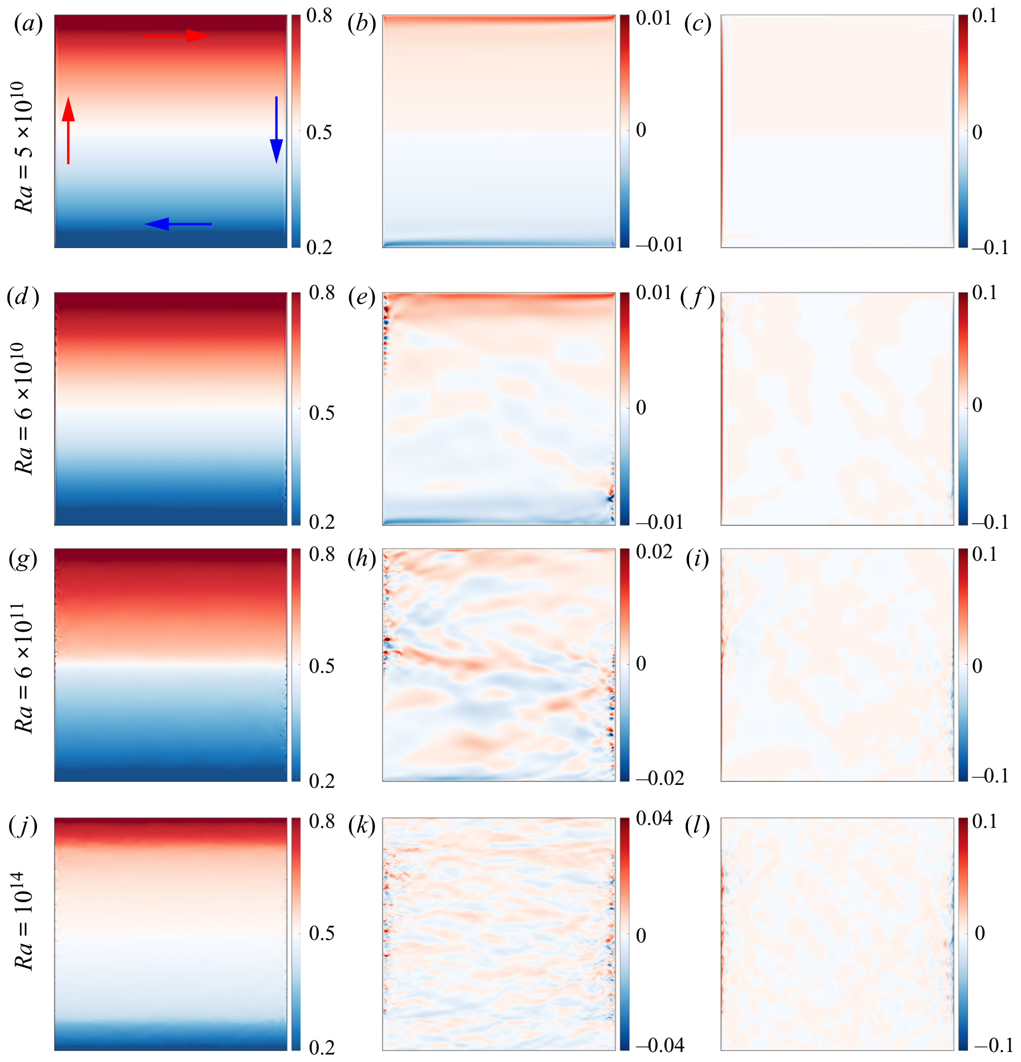

Figure 2. Instantaneous temperature θ (*a*,*d*,*g*,*j*), horizontal velocity u (*b*,*e*,*h*,*k*) and vertical velocity (*c*,*f*,*i*,*l*) fields for different Ra with $Pr = 10$ and $\Gamma = 1$. (*a–c*) Regime I where $Ra = 5 \times 10^{10}$. (*d–f*) Regime II where $Ra = 6 \times 10^{10}$. (*g–i*) Regime II where $Ra = 6 \times 10^{11}$. (*j–l*) Regime III where $Ra = 10^{14}$. The arrows in (*a*) indicate the velocity directions.

temperature gradient. Further prominent features are the ‘layered’ structures near the top and bottom walls, where relatively hot/cold fluids clearly separate from the near-isothermal bulk region.

3.2. *Mean profiles for temperature and horizontal velocity*

We have seen that the global flow organization evidently changes with increasing Ra. In this subsection, we quantify these changes by looking at the mean profiles for the temperature and for the horizontal velocity. Figure 3(*a*) clearly shows the change in the temperature profiles at $x/L = 0.5$ with increasing Ra, which is consistent with the temperature fields presented in figure 2. The change of the bulk temperature profile shape can be quantified by the time-averaged non-dimensional vertical temperature gradient

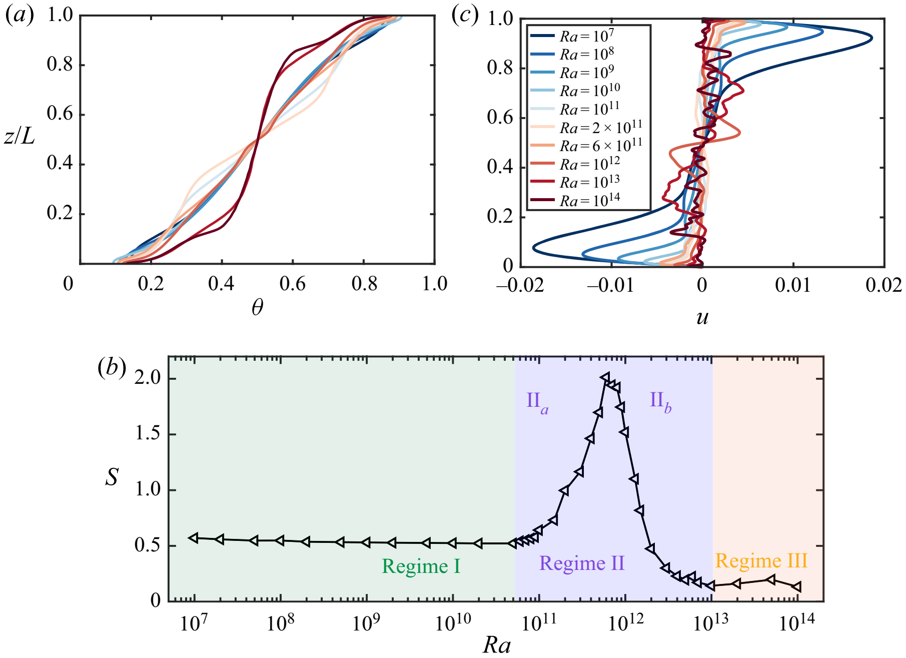

Figure 3. (a) Mean temperature profiles $\theta(z)$ at $x/L = 0.5$ for different Ra with $Pr = 10$. (b) Time-averaged centre vertical temperature gradient $S = \langle (L/\Delta)(\partial T/\partial z)_c \rangle_t$ as a function of Ra for $Pr = 10$. In regime I and regime III, S is weakly dependent on Ra. In contrast, in regime II, S displays a non-monotonic dependence on Ra. Regime II is further divided into II_a and II_b, in which S increases or decreases with increasing Ra, respectively. (c) Mean horizontal velocity profiles at $x/L = 0.5$ for different Ra with $Pr = 10$. Panels (a) and (c) share the same legend.

in the cell centre, i.e. $S \equiv \langle (L/\Delta)(\partial T/\partial z)_c \rangle_t$ (Paolucci 1990; Ravi *et al.* 1994). This quantity is plotted in figure 3(b), where one can observe three different regimes. In the well-explored regime I ($Ra \lesssim 5 \times 10^{10}$), S weakly depends on Ra, with a value $S \approx 0.5$, close to that of $S = 0.52$ for $Ra = 10^8$ with $Pr = 70$ reported in Ravi *et al.* (1994). However, in regime II ($5 \times 10^{10} \lesssim Ra \lesssim 10^{13}$), S has a non-monotonic dependence on Ra: it first increases with increasing Ra, reaches its maximum at $Ra = 6 \times 10^{11}$, and then decreases again. Regime II is further divided into regime II_a, where S increases with increasing Ra, and regime II_b, where S decreases with increasing Ra. The onset of regime II coincides with the onset of unsteadiness, which shows that plume emissions play an important role in altering the bulk properties. The maximum of S occurs when approximately half of sidewall areas (downstream) feature plume emissions, as shown in figure 2(g). Finally, in regime III, S again becomes weakly dependent on Ra, while it has a smaller value than that of regime I. The small value of S in regime III arises from the well-mixed bulk region, as can be seen in figure 2(j).

Figure 3(c) shows the change of the horizontal velocity profiles with increasing Ra. In regime I, the strong horizontal fluid motions concentrate near the top and bottom walls. In contrast, in regime III, the largest horizontal velocity appears in the bulk region, and alternating rightward and leftward fluid motions, i.e. zonal flows, are observed even after time averaging, which is consistent with the instantaneous horizontal velocity field shown in figure 2(k). Another prominent flow feature of regime III is that the horizontal velocity near the top and bottom walls is close to 0. This means that the 'layered structure' near the

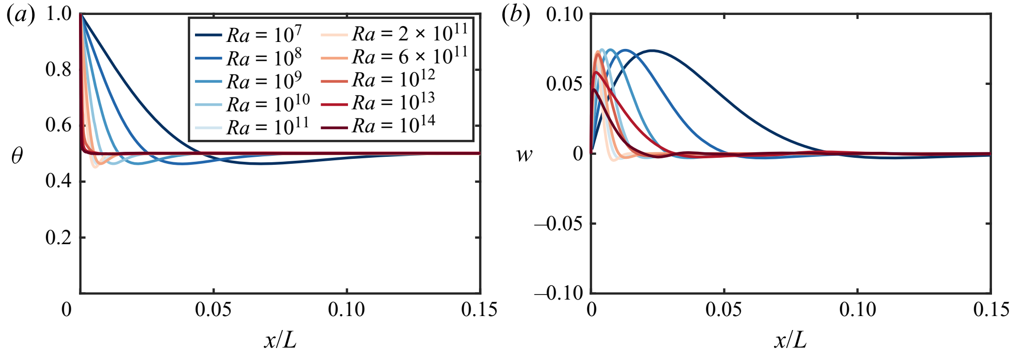

Figure 4. Mean (*a*) longitudinal temperature profile and (*b*) longitudinal profile of the vertical velocity at mid-height $z/L = 0.5$ for different Ra with $Pr = 10$. Panels (*a*) and (*b*) share the same legend.

top and bottom walls, as indicated in the temperature field in figure 2(*j*), is actually nearly a 'dead zone' with weak fluid motions. Thus the appearance of this nearly 'dead' layered structure indicates the the onset of regime III. Regime II serves to connect regime I and regime III: in regime II_a, the strongest horizontal motion still takes place near the top and bottom walls, see, e.g. the horizontal velocity profile for $Ra = 2 \times 10^{11}$ in figure 3(*c*). In contrast, in regime II_b, the strongest horizontal fluid motions appear in the bulk, see, e.g. the strong zonal flow motions in the central region for $Ra = 10^{12}$, as shown in figure 3(*c*). We remark that the zonal flow has been found in many geo- and astrophysical flows (Yano, Talagrand & Drossart 2003; Heimpel, Aurnou & Wicht 2005; Nadiga 2006), and it has also been extensively studied in RBC (Goluskin *et al.* 2014; Wang *et al.* 2020*a*; Zhang *et al.* 2020; Reiter *et al.* 2021). It is remarkable and interesting to also observe zonal flows in the high-*Ra* VC system. This system thus provides another model to study the physics of the zonal flow.

3.3. *Mean profiles for temperature and vertical velocity*

We now consider the mean vertical velocity and temperature profiles in the longitudinal (x) direction. Figure 4(*a*) shows the mean temperature profiles in the longitudinal (x) direction at mid-height $z/L = 0.5$ for different Ra. It is seen that for Ra values that are not too high, the temperature does not monotonically drop from $\theta = 1$ at the hot wall to $\theta = 0.5$ in the core. Instead, an undershoot phenomenon is observed. This phenomenon arises from the stable stratification in the bulk (Ravi *et al.* 1994) and can also be observed in the similarity solutions of the boundary layer equations for natural convection over a vertical hot wall in a stably stratified environment (Henkes & Hoogendoorn 1989). However, for $Ra \geq 10^{12}$, we find that the overshoot phenomenon disappears. This arises from the continuous emissions of hot plumes at mid-height $z/L = 0.5$ and beyond, as then the hot fluid directly touches the well-mixed bulk flow with small stratification.

Figure 4(*b*) shows vertical velocity profiles in the longitudinal direction, again at mid-height $z/L = 0.5$. With increasing Ra, the boundary layer becomes thinner and the peak vertical velocity becomes smaller. This finding reflects the different flow organizations in the different regimes: the emitted plumes in regimes II and III weaken the overall vertical fluid motions, as compared with the steady flow organization in regime I. This is also reflected in the $Re \sim Ra^{\gamma}$ scaling, as will be discussed below.

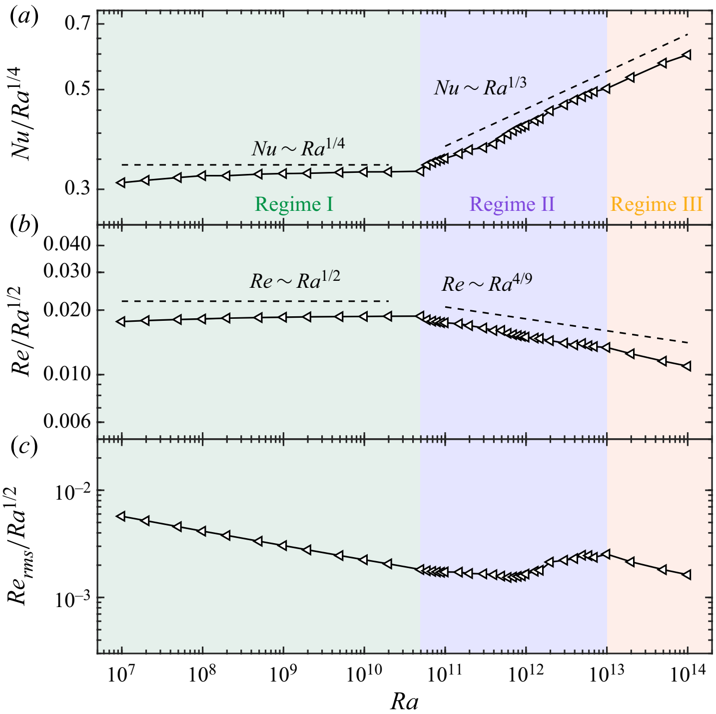

Figure 5. (a) Normalized Nusselt number $Nu/Ra^{1/4}$, (b) normalized Reynolds number based on maximal vertical velocity $Re/Ra^{1/2}$, and (c) normalized Reynolds number based on root-mean-square velocity $Re_{rms}/Ra^{1/2}$, as functions of Ra for $Pr = 10$. The solid lines connect the DNS data points, whereas the dashed lines show the suggested scaling laws. There is a clear and sharp transition in scaling between regime I and regime II/III.

4. Global heat and momentum transport and dissipation rates

Next, we focus on the global heat (Nu) and momentum (Re) transport. Here, we use the wind-based Reynolds number Re with the characteristic velocity

$$U_{max} \equiv \max_x H^{-1} \int_0^H w \, \mathrm{d}z, \tag{4.1}$$

which is the same definition as that in Shishkina (2016), and the root-mean-square Reynolds number Re_{rms} with the characteristic velocity

$$U_{rms} \equiv \sqrt{\langle \boldsymbol{u} \cdot \boldsymbol{u} \rangle_{V,t}}, \tag{4.2}$$

where $\langle \rangle_{V,t}$ indicates volume and time averaging. Figures 5(a) and 5(b) show that in regime I, the obtained effective power law scaling relations agree remarkably well with the theoretical prediction made for laminar VC (Shishkina 2016), namely, $Nu \sim Ra^{1/4}$ and $Re \sim Ra^{1/2}$. The fitted scaling relations are provided in table 1. It is also seen that a slightly faster growth of Nu with Ra is obtained for $Ra \leq 10^9$. A similar increase of the scaling exponent for small Ra has also been found previously in both confined (Shishkina 2016; Wang, Zhang & Guo 2017; Wang *et al.* 2019) and double periodic VC (Ng *et al.* 2015). However, when $Ra \geq 5 \times 10^{10}$, in regime II and regime III, evidently different scaling relations are observed. The fitted power law scaling relations (see table 1 for the obtained values) are close to $Nu \sim Ra^{1/3}$ (referred to as Malkus scaling Malkus 1954) and $Re \sim Ra^{4/9}$, which, interestingly, were predicted for regime IV$_u$ by the unifying

Regime	Ra range	Nu	Re	Re_{rms}	$\langle \epsilon_u \rangle / [L^{-4}\nu^3(Nu-1)RaPr^{-2}]$
Regime I	$[10^7, 5\times 10^{10}]$	$\sim Ra^{0.256}$	$\sim Ra^{0.507}$	$\sim Ra^{0.366}$	$\sim Ra^{-0.012}$
Regime II	$[5\times 10^{10}, 10^{13}]$	$\sim Ra^{0.330}$	$\sim Ra^{0.438}$	—	$\sim Ra^{-0.179}$
Regime III	$[10^{13}, 10^{14}]$	$\sim Ra^{0.326}$	$\sim Ra^{0.413}$	$\sim Ra^{0.310}$	$\sim Ra^{-0.248}$

Table 1. Fitted scaling relations of the Nusselt number Nu, the Reynolds number based on maximal vertical velocity Re (4.1), the Reynolds number based on root-mean-square velocity Re_{rms} (4.2) and the normalized kinetic dissipation rate $\langle \epsilon_u \rangle / [L^{-4}\nu^3(Nu-1)RaPr^{-2}]$ with respect to Ra for the three different regimes.

theory for RBC (Grossmann & Lohse 2000). Such observation of scaling transitions further demonstrates that there are no pure scaling laws in thermal convection. This has already been seen in RBC (Grossmann & Lohse 2000; Ahlers *et al.* 2009), horizontal convection (Shishkina *et al.* 2016; Shishkina & Wagner 2016; Reiter & Shishkina 2020) and internally heated convection (Wang *et al.* 2020*b*), and apparently crossovers between different scaling regimes also occur here. However, the sharpness of the scaling transition from $\beta = 1/4$ to $\beta = 1/3$ observed here is quite different from the smooth transition seen in RBC. Indeed, in RBC, the transition from $Nu \sim Ra^{1/4}$ to $Nu \sim Ra^{1/3}$ is very smooth, spread over more than two orders of magnitude in Ra (Grossmann & Lohse 2000), and the linear combination of the 1/4 and 1/3 power laws even mimics an effective 2/7 scaling exponent (Castaing *et al.* 1989) over many orders of magnitude in Ra.

Figure 5(*c*) shows that also Re_{rms} behaves differently in different regimes. The fitted scaling relation $Re_{rms} \sim Ra^{0.37}$ in regime I is the same as that found for 2-D VC with $Pr = 0.71$ (Wang *et al.* 2019), which suggests that in vertical convection, different Reynolds numbers have different scaling relations with Ra. In regime II, the normalized Reynolds number $Re_{rms}/Ra^{1/2}$ depends non-monotonically on Ra, and shows a pronounced local minimum. The fitted scaling exponent 0.31 in regime III is again smaller than that in regime I.

It is interesting to note that, though S shows a clear transition between regime II and regime III, this transition is not seen in the effective power law scaling relations $Nu \sim Ra^{\beta}$ and $Re \sim Ra^{\gamma}$. Our interpretation of this noteworthy finding is as follows. The transition of the flow organization from regime I to regime II is sharp in view of the sudden appearance of plume emissions from the sidewall thermal boundary layers, and in view of the emergence of the local minimum of the Nusselt number distribution on the sidewall. However, the transition of flow organization from regime II to regime III is more continuous. The flows in these two regimes are characterized by the alternating rightward and leftward fluid motions, i.e. zonal flows, in the bulk, and they all have plume emissions from the sidewall boundary layers and a local minimum of the Nusselt number distribution on the sidewall. The only prominent difference is the appearance of layered structures near the top and bottom plates in regime III. As this layered structure only concentrates in a small region near the top and bottom plates, the global effective scaling exponents of Nu and Re do not seem to be sensitive to the different flow organizations in regimes II and III.

To better understand the sudden change of the global heat transport properties at the transition to regime II, we now consider the wall heat flux, which is denoted by the local Nusselt number at the wall $Nu(z)|_{x=0,1} = \partial \langle \theta \rangle_t / \partial x|_{x=0,1}$. Figure 6(*a*) displays $Nu(z)|_{x=0}$ at the left wall, while $Nu(z)|_{x=1}$ at the right wall is not shown owing to the inherent symmetry of the system. For $Ra \leq 5 \times 10^{10}$, the local $Nu(z)|_{x=0}$ generally decreases monotonically with increasing heights z. The large local $Nu(z)|_{x=0}$ for small heights z is attributed to the fact that the hot fluid there is in direct contact with the cold fluid, which leads to large temperature gradients. In contrast, for $Ra > 5 \times 10^{10}$, a local minimum

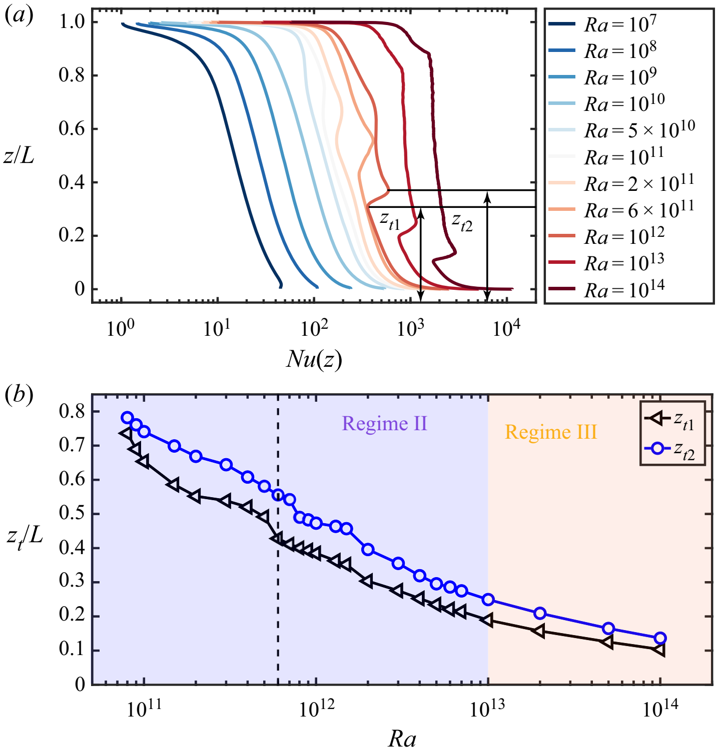

Figure 6. (a) Local Nusselt number $Nu(z)$ at the hot wall ($x/L = 0$) for different Ra, all with $Pr = 10$. (b) Transition points z_t/L as functions of Ra. Here, z_{t1} and z_{t2} are the locations where $Nu(z)$ reaches its local minimum and maximum values, respectively. Such local maximum and minimum occur beyond $Ra \gtrsim 5 \times 10^{10}$, see ($a$). The dashed vertical line denotes the Ra where the centre temperature gradient is maximal.

and a local maximum in $Nu(z)|_{x=0}$ are identified, the heights of which are denoted as z_{t1} and z_{t2}. It is clearly seen that $Nu(z)|_{x=0}$ after the first transition point z_{t1} increases compared with the steady cases at $Ra \leq 5 \times 10^{10}$. This is because the emissions of the plumes lead to more efficient shear-driven mixing, and therefore larger local $Nu(z)|_{x=0}$. Thus, the overall heat transport also increases in regime II and later regime III (figure 5a) owing the ejections of plumes, and the change of the scaling is also related to the change of the boundary layer properties.

We have shown that the two transition points z_{t1} and z_{t2} roughly correspond to the locations where plumes begin to be ejected. Figure 6(b) shows, as expected, that both z_{t1} and z_{t2} decrease with increasing Ra, which suggests that the locations where hot plumes begin to be ejected move downwards with increasing Ra. At $Ra = 6 \times 10^{11}$, where the centre temperature gradient S achieves its maximum, it can be seen that the mid-height $z/L = 0.5$ lies between the two transition points, further demonstrating that the maximum of S is achieved once plumes are ejected over approximately half of the area (downstream) of the sidewalls, as seen in the temperature field in figure 2(g).

Finally, we discuss the thermal and kinetic dissipation rates. In RBC, the following exact relations hold (Shraiman & Siggia 1990).

$$\langle \epsilon_u \rangle_V = \frac{\nu^3}{L^4}(Nu - 1)RaPr^{-2}, \tag{4.3}$$

$$\langle \epsilon_\theta \rangle_V = \kappa \frac{\varDelta^2}{L^2} Nu. \tag{4.4}$$

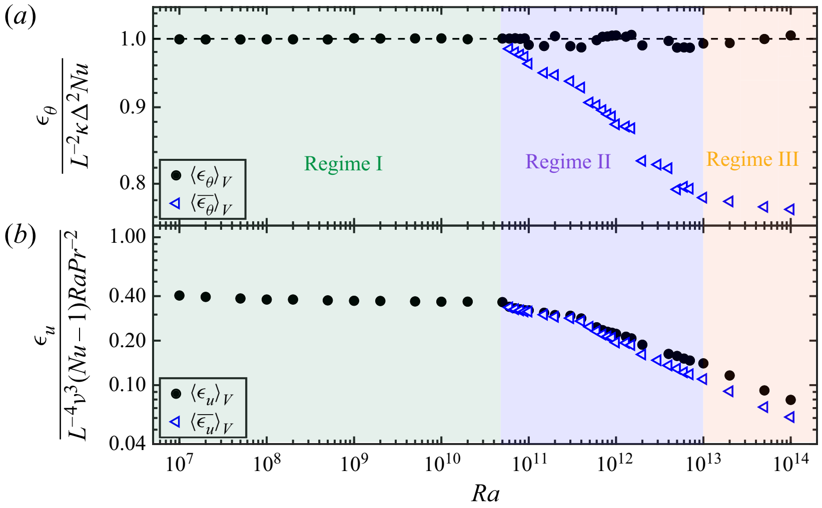

Figure 7. Normalized (*a*) thermal dissipation rate $\langle\epsilon_\theta\rangle/(L^{-2}\kappa\Delta^2 Nu)$ and (*b*) kinetic dissipation rate $\langle\epsilon_u\rangle/[L^{-4}\nu^3(Nu-1)RaPr^{-2}]$ as functions of *Ra*. The black solid circles denote the total dissipation rates while hollow triangles correspond the dissipation rates of the mean field.

The average $\langle\rangle_V$ is over the whole volume and over time. In VC, the relation (4.4) still holds, however, the relation (4.3) does not hold any longer. Following Ng *et al.* (2015) and Reiter & Shishkina (2020), we decompose the dissipation rates into their mean and fluctuating parts as $\langle\epsilon_u\rangle_V = \langle\overline{\epsilon_u}\rangle_V + \langle\epsilon'_u\rangle_V = \nu[\langle(\partial U_i/\partial x_j)^2\rangle_V + \langle(\partial u'_i/\partial x_j)^2\rangle_V]$. Figure 7(*a*) shows that the relation (4.4) is fulfilled in the DNS. It is also seen that the contribution from the mean field decreases with increasing *Ra*, which suggests that with increasing *Ra*, turbulent fluctuations play an increasingly more important role on the mixing process.

The kinetic dissipation rate is displayed in figure 7(*b*). One can see that the values $\langle\epsilon_u\rangle/[L^{-4}\nu^3(Nu-1)RaPr^{-2}]$ are always smaller than the corresponding value, as occurs in RBC. This was already seen in 3-D VC (Shishkina 2016). For the steady VC with $Ra \leq 5\times10^{10}$, the normalized kinetic dissipation rate only weakly depends on *Ra*, as has also been found in 3-D VC (Shishkina 2016). However, in regimes II and III, it is observed that the normalized kinetic dissipation rate decreases much faster than that in regime I. This can be related to the fact that *Nu* increases faster in regimes II and III than in regime I. It is also seen that the contribution from turbulent fluctuations is small, similar as in horizontal convection (Reiter & Shishkina 2020).

5. Conclusions

In conclusion, we have studied vertical convection by direct numerical simulations over seven orders of magnitude of Rayleigh numbers, i.e. $10^7 \leq Ra \leq 10^{14}$, for a fixed Prandtl number $Pr = 10$ in a two-dimensional convection cell with unit aspect ratio. The main conclusions, which correspond to the answers of the questions posed in the introduction, are summarized as follows.

(i) The dependence of the non-dimensional mean vertical temperature gradient at the cell centre *S* on *Ra* shows three different regimes. In regime I ($Ra \lesssim 5\times10^{10}$), *S* is almost independent of *Ra*, which is consistent with previous work (Paolucci 1990). However, in the newly identified regime II ($5\times10^{10} \lesssim Ra \lesssim 10^{13}$), *S* first increases with increasing *Ra*, reaches its maximum and then decreases again. In regime III ($Ra \gtrsim 10^{13}$), *S* again becomes weakly dependent on *Ra*, with a smaller value than that of regime I. The transition from regime I to regime II coincides with the onset of unsteady fluid motions. The maximum of *S* occurs when plumes are ejected over approximately half of the area of the sidewall, namely, in the downstream region. The flow in regime III is characterized by a well-mixed bulk region owing to continuous ejection of plumes over large fractions of the sidewalls. Thus *S* is smaller than that of regime I.

(ii) The flow organizations in the three different regimes are quite different from each other. In regime I, the maximal horizontal velocity concentrates near the top and bottom walls. However, the flow gives way to alternating rightward and leftward zonal flows in regime III, where the maximal horizontal velocity appears in the bulk region. Another characteristic feature of the flow in regime III are the 'layered' structures near the top and bottom walls, where the fluid motions are weak. Regime II serves to connect regime I and regime III: in regime II_a, the maximal velocity still occurs near the top and bottom walls. In contrast, in regime II_b, the zonal flow structures become more pronounced, and the maximal horizontal velocity is found in the bulk region.

(iii) Transitions in the scaling relations $Nu \sim Ra^{\beta}$ and $Re \sim Ra^{\gamma}$ are found. In regime I, the fitted scaling exponents ($\beta \approx 0.26$ and $\gamma \approx 0.51$) are in excellent agreement with the theoretical prediction of $\beta = 1/4$ and $\gamma = 1/2$ for the laminar VC (Shishkina 2016). However, β increases to a value close to 1/3 and γ decreases to a value close to 4/9 in regimes II and III. The increased heat transport *Nu* in regimes II and III is related to the ejection of plumes and larger local heat flux at the sidewalls. The mean kinetic dissipation rate also shows different scalings in the different regimes.

We note that the present study only focuses on $Pr = 10$. Further studies, both numerical simulations and experiments, are needed to address the influence of the Prandtl number *Pr* and the aspect ratio Γ on the regime transitions in the high-*Ra* vertical convection. The reported scaling relations for $Nu \sim Ra^{\beta}$ and $Re \sim Ra^{\gamma}$ and the observed transitions are however already an important ingredient to consider to develop a unifying scaling theory over a broad range of control parameters for vertical convection, to finally arrive at the full dependences $Nu(Ra, Pr)$ and $Re(Ra, Pr)$ and their theoretical understanding.

Acknowledgements. C.S. Ng, R.J.A.M. Stevens and K.L. Chong are gratefully acknowledged for discussions and support. We also acknowledge the Twente Max Planck Center, the Deutsche Forschungsgemeinschaft (Priority Programme SPP 1881 'Turbulent Superstructures'), PRACE for awarding us access to MareNostrum 4 based in Spain at the Barcelona Computing Center (BSC) under PRACE project 2020225335. The simulations were partly carried out on the national e-infrastructure of SURFsara, a subsidiary of SURF co-operation, the collaborative ICT organization for Dutch education and research.

Funding. Q.W. acknowledges financial support from the China Scholarship Council (CSC) and the Natural Science Foundation of China (NSFC) under grant no. 11621202.

Declaration of interests. The authors report no conflict of interest.

Author ORCIDs.
Qi Wang https://orcid.org/0000-0001-6986-3056;
Hao-Ran Liu https://orcid.org/0000-0001-7754-9454;
Roberto Verzicco https://orcid.org/0000-0002-2690-9998;
Olga Shishkina https://orcid.org/0000-0002-6773-6464;
Detlef Lohse https://orcid.org/0000-0003-4138-2255.

Appendix. Tables with simulation details

Ra	Pr	$N_x \times N_z$	Nu	Re	Re_{rms}	t_{avg}
10^7	10	256×256	17.45	55.91	18.07	s
2×10^7	10	256×256	21.01	79.94	23.22	s
5×10^5	10	256×256	26.79	127.81	32.32	s
10^8	10	256×256	32.17	181.76	41.49	s
2×10^8	10	512×512	38.25	259.57	53.56	s
5×10^8	10	512×512	48.48	412.66	74.76	s
10^9	10	512×512	57.83	585.72	96.28	s
2×10^9	10	1024×1024	68.87	831.61	124.19	s
5×10^9	10	1024×1024	86.97	1305.75	173.85	s
10^{10}	*10*	*512×512*	*104.10*	*1864.73*	*224.31*	*s*
10^{10}	10	1024×1024	103.72	1867.66	224.39	s
10^{10}	*10*	*2048×2048*	*103.57*	*1869.23*	*224.48*	*s*
2×10^{10}	10	2048×2048	123.38	2647.58	290.75	s
5×10^{10}	10	2048×2048	155.63	4191.51	406.88	s
6×10^{10}	10	2048×2048	168.23	4411.20	434.19	4000
7×10^{10}	10	2048×2048	177.07	4698.16	462.49	4000
8×10^{10}	10	2048×2048	184.72	4989.32	489.22	4000
9×10^{10}	10	2048×2048	191.77	5243.58	514.73	4000
10^{11}	10	2048×2048	197.76	5519.30	546.72	700
1.5×10^{11}	10	2048×2048	224.16	6688.48	666.80	600
2×10^{11}	10	2048×2048	245.75	7571.25	747.44	1000
3×10^{11}	10	4096×4096	274.91	9035.54	908.88	600
4×10^{11}	10	4096×4096	301.02	10157.67	1030.33	600
5×10^{11}	10	4096×4096	327.13	11371.01	1118.77	400
6×10^{11}	10	4096×4096	350.12	12071.13	1189.22	400
7×10^{11}	10	4096×4096	370.41	12852.20	1297.32	600
8×10^{11}	10	4096×4096	388.00	13599.04	1404.98	500
9×10^{11}	10	4096×4096	402.48	14329.93	1509.09	500
10^{12}	10	4096×4096	416.76	14969.80	1652.75	538
1.3×10^{12}	10	4096×4096	455.39	16886.46	2001.21	318
1.5×10^{12}	10	4096×4096	476.91	18047.30	2194.89	304
2×10^{12}	10	4096×4096	533.62	20368.53	3024.04	500
3×10^{12}	10	4096×4096	608.89	24315.69	3851.81	307
4×10^{12}	10	4096×4096	670.80	27518.31	4610.48	600
5×10^{12}	10	4096×4096	721.14	31241.75	5532.71	400
5×10^{12}	*10*	*6144×6144*	*719.14*	*30901.58*	*5549.52*	*200*
6×10^{12}	10	4096×4096	766.01	33418.22	6018.00	339
7×10^{12}	10	4096×4096	804.78	35765.90	6256.97	442
10^{13}	10	6144×6144	894.12	42328.91	8008.78	170
10^{13}	*10*	*4096×4096*	*896.63*	*43023.82*	*7955.93*	*400*
2×10^{13}	10	6144×6144	1125.87	55947.28	9598.67	250
5×10^{13}	10	6144×6144	1523.18	81719.17	12837.24	200
10^{14}	10	8192×8192	1890.36	109546.69	16289.48	160
10^{14}	*10*	*6144×6144*	*1907.95*	*109022.39*	*16615.48*	*150*

Table 2. The columns from left to right indicate the following: the Rayleigh number Ra, the Prandtl number Pr, the grid resolution $N_x \times N_z$, the Nusselt number Nu, the Reynolds number based on maximal vertical velocity Re (averaged over horizontal direction), the Reynolds number based on root-mean-square velocity Re_{rms}, the time t_{avg} used to average Nu and Re. The aspect ratio is fixed to 1 for all the cases. ‘s’ means that the flow is steady. Cases indicated in blue and italic are used for grid independence checks. We note that the difference of Nu for two different grids is always smaller than 1 %, and the difference of Re for the different grids is always smaller than 2 %.

REFERENCES

AHLERS, G., GROSSMANN, S. & LOHSE, D. 2009 Heat transfer and large scale dynamics in turbulent Rayleigh-Bénard convection. *Rev. Mod. Phys.* **81**, 503–537.

BATCHELOR, G.K. 1954 Heat transfer by free convection across a closed cavity between vertical boundaries at different temperatures. *Q. Appl. Maths* **12**, 209–233.

BLYTHE, P.A., DANIELS, P.G. & SIMPKINS, P.G. 1983 Thermal convection in a cavity: the core structure near the horizontal boundaries. *Proc. R. Soc. Lond.* A **387**, 367–388.

CASTAING, B., GUNARATNE, G., HESLOT, F., KADANOFF, L., LIBCHABER, A., THOMAE, S., WU, X.-Z., ZALESKI, S. & ZANETTI, G. 1989 Scaling of hard thermal turbulence in Rayleigh–Bénard convection. *J. Fluid Mech.* **204**, 1–30.

CHENOWETH, D.R. & PAOLUCCI, S 1986 Natural convection in an enclosed vertical air layer with large horizontal temperature differences. *J. Fluid Mech.* **169**, 173–210.

CHILLÀ, F. & SCHUMACHER, J. 2012 New perspectives in turbulent Rayleigh-Bénard convection. *Eur. Phys. J.* E **35**, 58.

CHONG, K.L., YANG, R., WANG, Q., VERZICCO, R. & LOHSE, D. 2020 Café Latte: spontaneous layer formation in laterally cooled double diffusive convection. *J. Fluid Mech.* **900**, R6.

GILL, A.E. 1966 The boundary-layer regime for convection in a rectangular cavity. *J. Fluid Mech.* **26**, 515–536.

GOLUSKIN, D., JOHNSTON, H., FLIERL, G.R. & SPIEGEL, E.A. 2014 Convectively driven shear and decreased heat flux. *J. Fluid Mech.* **759**, 360–385.

GRAEBEL, W.P. 1981 The influence of Prandtl number on free convection in a rectangular cavity. *Intl J. Heat Mass Transfer* **24**, 125–131.

GROSSMANN, S. & LOHSE, D. 2000 Scaling in thermal convection: a unifying theory. *J. Fluid Mech.* **407**, 27–56.

GROSSMANN, S. & LOHSE, D. 2001 Thermal convection for large prandtl numbers. *Phys. Rev. Lett.* **86**, 3316.

GROSSMANN, S. & LOHSE, D. 2002 Prandtl and Rayleigh number dependence of the Reynolds number in turbulent thermal convection. *Phys. Rev.* E **66**, 016305.

GROSSMANN, S. & LOHSE, D. 2004 Fluctuations in turbulent Rayleigh–Bénard convection: the role of plumes. *Phys. Fluids* **16**, 4462–4472.

GUO, S.-X., ZHOU, S.-Q., CEN, X.-R., QU, L., LU, Y.-Z., SUN, L. & SHANG, X.-D. 2015 The effect of cell tilting on turbulent thermal convection in a rectangular cell. *J. Fluid Mech.* **762**, 273–287.

HADLEY, G. 1735 Concerning the cause of the general trade-winds. *Phil. Trans. R. Soc. Lond.* **39**, 58–62.

HEIMPEL, M., AURNOU, J. & WICHT, J. 2005 Simulation of equatorial and high-latitude jets on Jupiter in a deep convection model. *Nature* **438**, 193–196.

HENKES, R.A.W.M. & HOOGENDOORN, C.J. 1989 Laminar natural convection boundary-layer flow along a heated vertical plate in a stratified environment. *Intl J. Heat Mass Transfer* **32**, 147–155.

JANSSEN, R.J.A. & HENKES, R.A.W.M. 1995 Influence of prandtl number on instability mechanisms and transition in a differentially heated square cavity. *J. Fluid Mech.* **290**, 319–344.

LAPPA, M. 2009 *Thermal Convection: Patterns, Evolution and Stability*. John Wiley & Sons.

LE QUÉRÉ, P. & BEHNIA, M. 1998 From onset of unsteadiness to chaos in a differentially heated square cavity. *J. Fluid Mech.* **359**, 81–107.

LIU, H.-R., CHONG, K.L., WANG, Q., NG, C.S., VERZICCO, R. & LOHSE, D. 2021 Two-layer thermally driven turbulence: mechanisms for interface breakup. *J. Fluid Mech.* **913**, A9.

LOHSE, D. & XIA, K.-Q. 2010 Small-scale properties of turbulent Rayleigh–Bénard convection. *Annu. Rev. Fluid Mech.* **42**, 335–364.

MALKUS, W.V.R. 1954 The heat transport and spectrum of thermal turbulence. *Proc. R. Soc. Lond.* A **225** (1161), 196–212.

NADIGA, B.T. 2006 On zonal jets in oceans. *Geophys. Res. Lett.* **33**, L10601.

NG, C.S., OOI, A., LOHSE, D. & CHUNG, D. 2015 Vertical natural convection: application of the unifying theory of thermal convection. *J. Fluid Mech.* **764**, 349–361.

NG, C.S., OOI, A., LOHSE, D. & CHUNG, D. 2017 Changes in the boundary-layer structure at the edge of the ultimate regime in vertical natural convection. *J. Fluid Mech.* **825**, 550–572.

NG, C.S., OOI, A., LOHSE, D. & CHUNG, D. 2018 Bulk scaling in wall-bounded and homogeneous vertical natural convection. *J. Fluid Mech.* **841**, 825–850.

NG, C.S., SPANDAN, V., VERZICCO, R. & LOHSE, D. 2020 Non-monotonic transport mechanisms in vertical natural convection with dispersed light droplets. *J. Fluid Mech.* **900**, A34.

PAOLUCCI, S. 1990 Direct numerical simulation of two-dimensional turbulent natural convection in an enclosed cavity. *J. Fluid Mech.* **215**, 229–262.

PAOLUCCI, S. & CHENOWETH, D.R. 1989 Transition to chaos in a differentially heated vertical cavity. *J. Fluid Mech.* **201**, 379–410.

van der Poel, E.P., Ostilla-Mónico, R., Donners, J. & Verzicco, R. 2015 A pencil distributed finite difference code for strongly turbulent wall-bounded flows. *Comput. Fluids* **116**, 10–16.

Ravi, M.R., Henkes, R.A.W.M. & Hoogendoorn, C.J. 1994 On the high-Rayleigh-number structure of steady laminar natural-convection flow in a square enclosure. *J. Fluid Mech.* **262**, 325–351.

Reiter, P. & Shishkina, O. 2020 Classical and symmetrical horizontal convection: detaching plumes and oscillations. *J. Fluid Mech.* **892**, R1.

Reiter, P., Zhang, X., Stepanov, R. & Shishkina, O. 2021 Generation of zonal flows in convective systems by travelling thermal waves. *J. Fluid Mech.* **913**, A13.

Sebilleau, F., Issa, R., Lardeau, S. & Walker, S.P. 2018 Direct numerical simulation of an air-filled differentially heated square cavity with rayleigh numbers up to 1011. *Intl J. Heat Mass Transfer* **123**, 297–319.

Shishkina, O. 2016 Momentum and heat transport scalings in laminar vertical convection. *Phys. Rev.* E **93**, 051102.

Shishkina, O., Grossmann, S. & Lohse, D. 2016 Heat and momentum transport scalings in horizontal convection. *Geophys. Res. Lett.* **43**, 1219–1225.

Shishkina, O. & Horn, S. 2016 Thermal convection in inclined cylindrical containers. *J. Fluid Mech.* **790**, R3.

Shishkina, O., Stevens, R.J.A.M., Grossmann, S. & Lohse, D. 2010 Boundary layer structure in turbulent thermal convection and its consequences for the required numerical resolution. *New J. Phys.* **12**, 075022.

Shishkina, O. & Wagner, S. 2016 Prandtl-number dependence of heat transport in laminar horizontal convection. *Phys. Rev. Lett.* **116**, 024302.

Shraiman, B.I. & Siggia, E.D. 1990 Heat transport in high-Rayleigh-number convection. *Phys. Rev.* A **42**, 3650.

Stevens, R.J.A.M., van der Poel, E.P., Grossmann, S. & Lohse, D. 2013 The unifying theory of scaling in thermal convection: the updated prefactors. *J. Fluid Mech.* **730**, 295–308.

Tanny, J. & Tsinober, A.B. 1988 The dynamics and structure of double-diffusive layers in sidewall-heating experiments. *J. Fluid Mech.* **196**, 135–156.

Thorpe, S.A., Hutt, P.K. & Soulsby, R. 1969 The effect of horizontal gradients on thermohaline convection. *J. Fluid Mech.* **38** (2), 375–400.

Trias, F.X., Gorobets, A., Soria, M. & Oliva, A. 2010 Direct numerical simulation of a differentially heated cavity of aspect ratio 4 with Rayleigh numbers up to $10^1$1–Part I: Numerical methods and time-averaged flow. *Intl J. Heat Mass Transfer* **53**, 665–673.

Trias, F.X., Soria, M., Oliva, A. & Pérez-Segarra, C.D. 2007 Direct numerical simulations of two-and three-dimensional turbulent natural convection flows in a differentially heated cavity of aspect ratio 4. *J. Fluid Mech.* **586**, 259–293.

de Vahl Davis, G. & Jones, I.P. 1983 Natural convection in a square cavity: a comparison exercise. *Intl J. Numer. Meth. Fluids* **3**, 227–248.

Verzicco, R & Orlandi, P 1996 A finite-difference scheme for three-dimensional incompressible flows in cylindrical coordinates. *J. Comput. Phys.* **123**, 402–414.

Wang, P., Zhang, Y. & Guo, Z. 2017 Numerical study of three-dimensional natural convection in a cubical cavity at high Rayleigh numbers. *Intl J. Heat Mass Transfer* **113**, 217–228.

Wang, Q., Chong, K.-L., Stevens, R.J.A.M., Verzicco, R. & Lohse, D. 2020*a* From zonal flow to convection rolls in Rayleigh–Bénard convection with free-slip plates. *J. Fluid Mech.* **905**, A21.

Wang, Q., Shishkina, O. & Lohse, D. 2020*b* Scaling in internally heated convection: a unifying theory. *Geophys. Res. Lett.* **48**, e2020GL091198.

Wang, Q., Verzicco, R., Lohse, D. & Shishkina, O. 2020*c* Multiple states in turbulent large-aspect ratio thermal convection: what determines the number of convection rolls? *Phys. Rev. Lett.* **125**, 074501.

Wang, Q., Wan, Z.-H., Yan, R. & Sun, D.-J. 2018*a* Multiple states and heat transfer in two-dimensional tilted convection with large aspect ratios. *Phys. Rev. Fluid* **3**, 113503.

Wang, Q., Xia, S.-N., Wang, B.-F., Sun, D.-J., Zhou, Q. & Wan, Z.-H. 2018*b* Flow reversals in two-dimensional thermal convection in tilted cells. *J. Fluid Mech.* **849**, 355–372.

Wang, Q., Xia, S.-N., Yan, R., Sun, D.-J. & Wan, Z.-H. 2019 Non-Oberbeck-Boussinesq effects due to large temperature differences in a differentially heated square cavity filled with air. *Intl J. Heat Mass Transfer* **128**, 479–491.

Xia, K.-Q. 2013 Current trends and future directions in turbulent thermal convection. *Theor. Appl. Mech. Lett.* **3**, 052001.

Xin, S. & Le Quéré, P. 1995 Direct numerical simulations of two-dimensional chaotic natural convection in a differentially heated cavity of aspect ratio 4. *J. Fluid Mech.* **304**, 87–118.

YANO, J.-I., TALAGRAND, O. & DROSSART, P. 2003 Outer planets: origins of atmospheric zonal winds. *Nature* **421**, 36.

ZHANG, L., DING, G.-Y. & XIA K.-Q. 2021 On the effective horizontal buoyancy in turbulent thermal convection generated by cell tilting. *J. Fluid Mech.* **914**, A15.

ZHANG, X., VAN GILS, D.P.M., HORN, S., WEDI, M., ZWIRNER, L., AHLERS, G., ECKE, R.E., WEISS, S., BODENSCHATZ, E. & SHISHKINA, O. 2020 Boundary zonal flow in rotating turbulent Rayleigh–Bénard convection. *Phys. Rev. Lett.* **124**, 084505.

ZWIRNER, L., KHALILOV, R., KOLESNICHENKO, I., MAMYKIN, A., MANDRYKIN, S., PAVLINOV, A., SHESTAKOV, A., TEIMURAZOV, A., FRICK, P. & SHISHKINA, O. 2020 The influence of the cell inclination on the heat transport and large-scale circulation in liquid metal convection. *J. Fluid Mech.* **884**, A18.

ZWIRNER, L. & SHISHKINA, O. 2018 Confined inclined thermal convection in low-Prandtl-number fluids. *J. Fluid Mech.* **850**, 984–1008.